

Article

Hot Rolling on Microstructure and Properties of NbHfTiVC_{0.1} Refractory High-Entropy Alloy

Haochen Qiu^{1,2,3}, Shutian Tao^{1,2,3}, Wei Jiang^{1,3}, Xuehui Yan^{1,3}, Shuaishuai Wu^{1,3}, Shengli Guo^{1,2,3}, Baohong Zhu^{1,2,3,*} and Dongxin Wang⁴

¹ GRIMAT Engineering Institute Co., Ltd., Beijing 101407, China; qiuhaochen@grinm.com (H.Q.); taoshutian@grinm.com (S.T.); jiangwei@grinm.com (W.J.); yanxuehui@grinm.com (X.Y.); wushuaishuai@grinm.com (S.W.); guoshengli@grinm.com (S.G.)

² General Research Institute for Nonferrous Metals, Beijing 100088, China

³ China GRINM Group Co., Ltd., Beijing 100088, China

⁴ State Key Laboratory of Special Rare Metal Materials, Northwest Rare Metal Materials Research Institute Ningxia Co., Ltd., Shizuishan 753000, China; wangdongxin123@126.com

* Correspondence: zhuhb@grinm.com; Tel./Fax: +86-010-60662898

Abstract: NbHfTiVC_{0.1} refractory high-entropy alloy (RHEA) exhibits excellent comprehensive mechanical properties and demonstrates great potential for applications. However, the mechanical properties need to be improved further. In this work, hot rolling on NbHfTiVC_{0.1} RHEA at temperatures of 650 °C, 850 °C, and 1050 °C, with total reductions of up to 30%, 50%, 70%, and 80%, was conducted. The microstructure and mechanical property evolution of the samples were further investigated. The hot-rolled samples at 650 °C and 850 °C exhibit a composition consisting of BCC, carbide, and Laves phases, whereas the samples rolled at 1050 °C only consist of BCC and carbide phases. The 650-80 sample displays the highest ultimate tensile strength (1354 MPa), and the 1050-80 sample demonstrates the highest elongation (16%). The highest strength observed in the 650 °C-80% sample can be attributed to the presence of fractured and refined carbides, fine-grains, and the hindrance of dislocation slip by the fine Laves phase. At a higher rolling temperature (1050 °C), the Laves phase disappears, resulting in a reduction in strength but an increase in plasticity. Furthermore, the dislocation slipping mechanism within the BCC matrix also contributes positively to plastic deformation, leading to a notable increase in ductility for the 1050 °C-80% sample. These research findings provide valuable insights into enhancing the strength and ductility simultaneously of NbHfTiVC_{0.1} RHEA through hot rolling.

Keywords: RHEAs; hot rolling; dislocation; microstructure; mechanical properties



Citation: Qiu, H.; Tao, S.; Jiang, W.; Yan, X.; Wu, S.; Guo, S.; Zhu, B.; Wang, D. Hot Rolling on Microstructure and Properties of NbHfTiVC_{0.1} Refractory High-Entropy Alloy. *Metals* **2023**, *13*, 1909. <https://doi.org/10.3390/met13111909>

Academic Editors: Martin Heilmaier and Babak Shalchi Amirkhiz

Received: 11 October 2023
Revised: 15 November 2023
Accepted: 16 November 2023
Published: 20 November 2023



Copyright: © 2023 by the authors. Licensee MDPI, Basel, Switzerland. This article is an open access article distributed under the terms and conditions of the Creative Commons Attribution (CC BY) license (<https://creativecommons.org/licenses/by/4.0/>).

1. Introduction

The need for materials suitable for high-temperature applications has always been a crucial demand. Many materials, such as Ni-based, Co-based, and Fe-based superalloys, have been utilized for the same purpose [1,2]. Nevertheless, their limitations in terms of thermal stability and melting point (1300 °C) have necessitated the development of novel materials [3–5]. The development of superalloys for higher exposure temperatures necessitates excellent softening resistance and phase stability and, consequently, materials capable of withstanding ever-increasing extreme operating conditions [4–6].

The concept of high-entropy alloys (HEAs) and multicomponent alloys was introduced in 2004, challenging the traditional belief that alloys were composed of one or two dominant elements [7–9]. High-entropy alloys, which are near-equimolar-composition alloys comprising five or more principal elements, have been roughly divided into two groups according to the different constituent elements [9–11]: one is based on 3d transition metals Co, Cr, Cu, Fe, Mn, Ni, Ti, and V, which are called TM HEAs; the other is refractory HEAs (RHEAs) [12–14].

Senkov et al. introduced refractory high-entropy alloys (RHEAs) in 2010. The RHEAs comprise refractory elements like Ti, V, Cr, Zr, Nb, Mo, Hf, Ta, and W, and exhibit outstanding qualities, including high strength at elevated temperatures and exceptional resistance to chemical corrosion [15–17]. The characteristics make them promising for a wide range of applications, including aviation, space engineering, engine manufacturing, chemical processing, and nuclear power plant technologies, where high-temperature requirements are significant [18–20]. Nevertheless, the limitations associated with the extremely low plasticity significantly impede their extensive use as structural materials in complex engineering environments [21–24]. For example, HfNbTiZr, TiZrHfTaW, MoNbReTaW, MoNbVTa, and TiVNbTaSi, etc., exhibit very high strength but poor ductility at room temperature [24–28]. Therefore, it is essential to improve the strength and ductility of the RHEAs.

Recently, a new class of carbon-doped NbHfTiV refractory high-entropy alloy was developed. The RHEAs perform outstanding strength and excellent ductility simultaneously [29]. However, the mechanical properties need to be improved further. In order to further improve mechanical properties and close defects retained during the initial fabrication, numerous endeavors have been made [30–32]. Suitable hot rolling processing is an efficient way and has been verified by a mass of reports, compared to cold rolling, which may cause excessive deformation resistance and sever the rebound of the material [33–35]. Additionally, hot-rolling allows for a higher formability of alloys into sheets and rods, and is thus commonly implemented during large-scale production [36–38]. However, rare studies have focused on the microstructural evolution and mechanical properties of the hot-rolling NbHfTiVC_{0.1} refractory high-entropy alloy (RHEA).

In the present work, the microstructure evolution of NbHfTiVC_{0.1} refractory high-entropy alloy during the hot rolling process was investigated. Additionally, the corresponding room temperature tensile properties were tested. It is expected to provide some reference for the research of hot rolling and other secondary processing on NbHfTiVC_{0.1} refractory high-entropy alloy.

2. Materials and Methods

2.1. Material Processing

The ingots of NbHfTiVC_{0.1} RHEAs were prepared via arc vacuum melting. The nominal purity of raw materials (Hf, V, Nb, and Ti) was above 99.5 at%, and the carbon was introduced into the alloy in the form of niobium carbide (NbC, 2–4 μm, 99.5 at%) intermediate alloy. The raw materials were weighed on an analytical balance (FA500) with an accuracy of 0.0001. The NbC powder was wrapped into titanium foil and placed at the bottom of a water-cooled copper crucible, while other raw materials were placed in the crucible from the bottom to top according to the ascending order of melting point.

To ensure chemical homogeneity, each ingot (~1000 g) was remelted five times and kept in the liquid state for 10 min during each remelting cycle before it was flipped for next remelting. The melt was eventually cast in a water-cooled copper mold to form a hemispherical ingot with dimensions of 80 mm.

The samples used for the subsequent hot rolling processes were cut from the ingot by electrical discharge machining with a size of 50 × 20 × 10 mm³. For consistency, all of the samples were located in regions with almost the same distance from the center of ingots.

2.2. Hot Rolling Processes

The samples were encapsulated in 304 stainless steel cans. After packaging, the samples were rolled on a hot rolling mill with a roller dimension of Φ 200 × 300 mm. The samples were preheated at 650 °C, 850 °C, and 1050 °C for 30 min before rolling to ensure the practical rolling temperature up to dynamic crystallization (DRX) temperature. In addition, the samples were reheated at 650 °C, 850 °C, and 1050 °C for 15 min during each pass to mitigate the temperature drop between the sample and rollers. The samples were cooled to room temperature in the air after reaching the target deformation. The sample was eight-passes rolled with a total reduction of 30% (650-30, 850-30, 1050-30), 50%

(650-50, 850-50, 1050-50), 70% (650-70, 850-70, 1050-70), and 80% (650-80, 850-80, 1050-80). Subsequently, the samples were removed from the cans.

2.3. Tensile Test

The tensile tests were performed on dog-bone-shaped specimens with a thickness of 1 mm and gauge length and width of 10 mm and 3.5 mm, respectively. In accordance with the GB/T 228.1 standard [39], the tensile properties were evaluated using a universal testing machine (MTS E45.105) at room temperature with a strain rate of 0.015 mm/min prior to the yield point and 4.8 mm/min after the yield point. The direction of the tensile test sample is according to the rolling direction. Three parallel samples were tested to obtain the average values of the results.

2.4. Microstructural Characterization

Specimens with dimensions of 10 mm × 10 mm × 10 mm were used for microstructure and phase analysis. The phase constitution of the alloys was determined via X-ray diffraction (XRD, D/max-RB) at 30 kV with Cu K α radiation. The XRD measurements were conducted at a step size of 4° for a range of 30–90°. Scanning electron microscopy (SEM, JSM-7900F, JEOL, Tokyo, Japan) equipped with energy dispersive X-ray spectroscopy (EDS) was performed to observe the morphology and microstructure of the alloys. The chemical composition of alloys was identified using energy dispersive X-ray spectroscopy (EDS). Grain distribution was investigated via SEM coupled with an electron backscatter diffraction (EBSD, JSM7001, JEOL, Tokyo, Japan) detector. Transmission electron microscopy (TEM, Tecnai G2 F20, FEI, Brno, Czech Republic) was utilized to identify microstructure of the alloys.

3. Results

3.1. Microstructure Evolution

The as-cast alloy consisted of BCC phase (black) and FCC-MC carbide phase (white) from a previous study [29]. Figure 1a shows the XRD results of hot-rolled samples at 650 °C, 850 °C, and 1050 °C for a 30% reduction. Figure 1b presents an enlarged view of the Laves peaks within the 2 θ angle range from 41° to 46°. As the hot rolling temperatures increased, the peaks corresponding to Laves phases gradually appeared at 850 °C, and disappeared at 1050 °C. Therefore, the hot-rolled samples at 850 °C are composed of BCC, carbide, and Laves phases, while the samples rolled at 650 °C and 1050 °C consist of BCC and carbide phases.

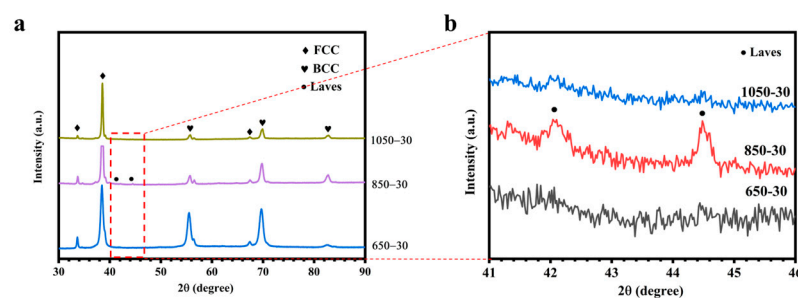


Figure 1. (a) XRD results of hot-rolled samples at 650 °C, 850 °C, and 1050 °C for 30% reduction; (b) enlarged peaks of the Laves phase.

Figures 2–4 depict the microstructure of hot-rolled NbHfTiVC_{0.1} samples at 650 °C, 850 °C, and 1050 °C for 30%, 50%, 70%, and 80% reductions. From the results, under the lowest rolling deformation amounts of 30% and 50%, the carbides still maintain block-like characteristic, and cracks with a 10 μ m length appear. However, for the higher rolling reductions (70%), the carbides are crushed into small pieces along the rolling direction. Moreover, under the highest rolling deformation amounts of 80% (650-80, 850-80, 1050-80),

the refinement of carbides is more pronounced and uniformly distributed in a chain pattern along the rolling direction, with an average size of 0.5–5 μm .

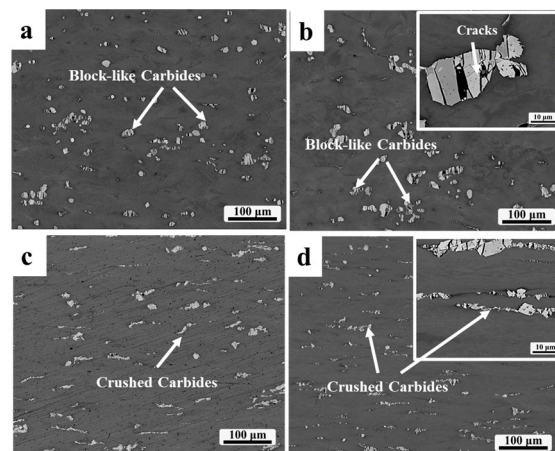


Figure 2. Microstructure of hot-rolled NbHfTiVC_{0.1} samples at 650 °C with the reductions: (a) 30%, (b) 50%, (c) 70%, (d) 80%.

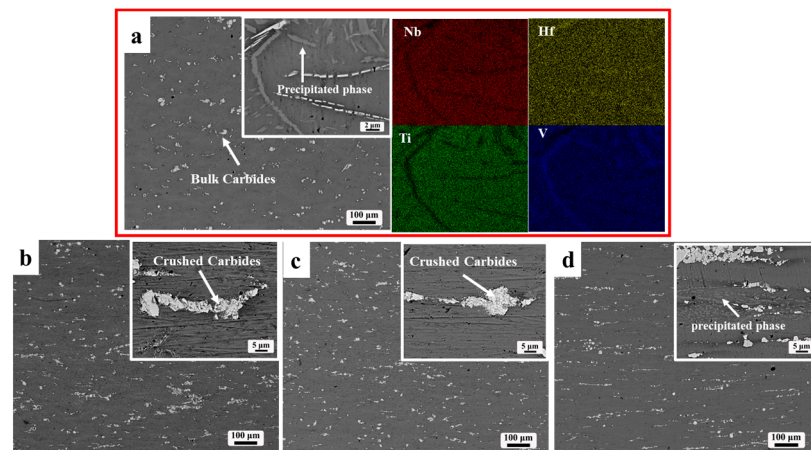


Figure 3. Microstructure of hot-rolled NbHfTiVC_{0.1} samples at 850 °C with the reductions: (a) 30%, (b) 50%, (c) 70%, (d) 80%.

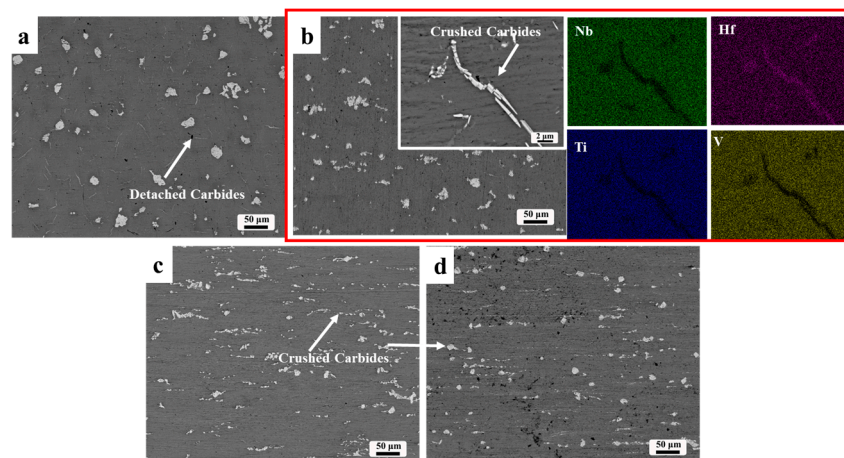


Figure 4. Microstructure of hot-rolled NbHfTiVC_{0.1} samples at 1050 °C with the reductions: (a) 30%, (b) 50%, (c) 70%, (d) 80%.

In addition to the rolling reduction amounts, rolling temperature is also an important factor influencing the composition and distribution of the phases. The refinement level of the carbide phase is not only affected by the rolling reductions, but also closely associated with the temperature. As shown in Figures 3 and 4, with the increase in rolling temperature, the refinement of the carbides becomes more pronounced. This leads to the separation of small carbide particles from the bulk carbides, causing them to disperse throughout the BCC matrix. This indicates that with the increase in the hot rolling temperature, the carbide phase softens, making it easier to fracture and refine, and then disperse in the alloy matrix. Furthermore, a large number of precipitated phases is generated in the BCC matrix at 850 °C, which is evenly distributed in grainy or strip shapes on both sides of the grain boundaries. However, the precipitated phases disappear in hot-rolled samples at 1050 °C.

Figures 3a and 4b depict the element distribution of the sample. The compositional distribution characteristics are visualized as follows: Nb, Hf, Ti, and V are distributed uniformly in the BCC matrix phase, while the precipitated phase (grey phase) is abundant in Hf and V. Additionally, the Hf is enriched in the carbide regions (white phase), as shown in Figure 4b.

To further provide insight into the phase constitution, a TEM observation of the tensile samples (850-80, 1050-80) at room temperature was conducted and the results are shown in Figure 5. A selected-area electron diffraction pattern (SAED) of the matrix phase is taken along the $[1\ 0\ 0]$ zone of the BCC structure, while the SAED pattern of the nano-precipitate phase is conducted along the $[1\ 1\ 0]$ zone of the HfV_2 (Laves phase). Furthermore, the phase (indicated by green line) is confirmed to be HfC carbides as shown in Figure 5b.

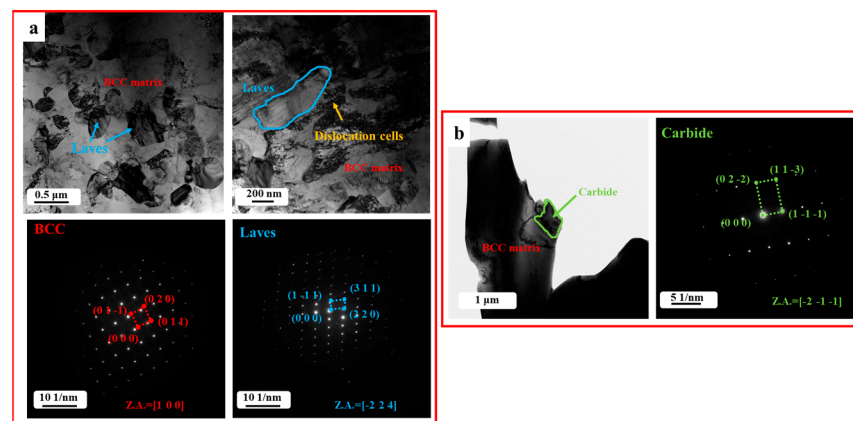


Figure 5. TEM observation of (a) 850-80 and (b) 1050-80 samples after tensile tests.

To study the microstructure evolution during the hot rolling process, an EBSD analysis was carried out on hot rolling at 650 °C and 850 °C, and the results are shown in Figures 6–9. EBSD maps of the 650-30, 650-50, and 650-80 samples are shown in Figure 6. In the 650-30 sample, a significant number of equiaxed grains are observed, while a smaller proportion of grains exhibits elongation parallel to the rolling direction. Moreover, paralleled twinning has been observed in the sample. From the enlarged image (Figure 7), it is noticeable that the twinned layer with a thickness of 2–5 μm is created at an angle of 40° in the rolling direction (indicated by the arrow). For the 650-50 sample, a significant number of grains also experienced deflection and elongation. This led to a predominant orientation of the grains along the $\langle 1\ 1\ 1 \rangle$ axis, indicated by the blue color. In the 650-80 sample, both equiaxed and elongated grains disappeared, while the presence of parallel recrystallized grains became evident.

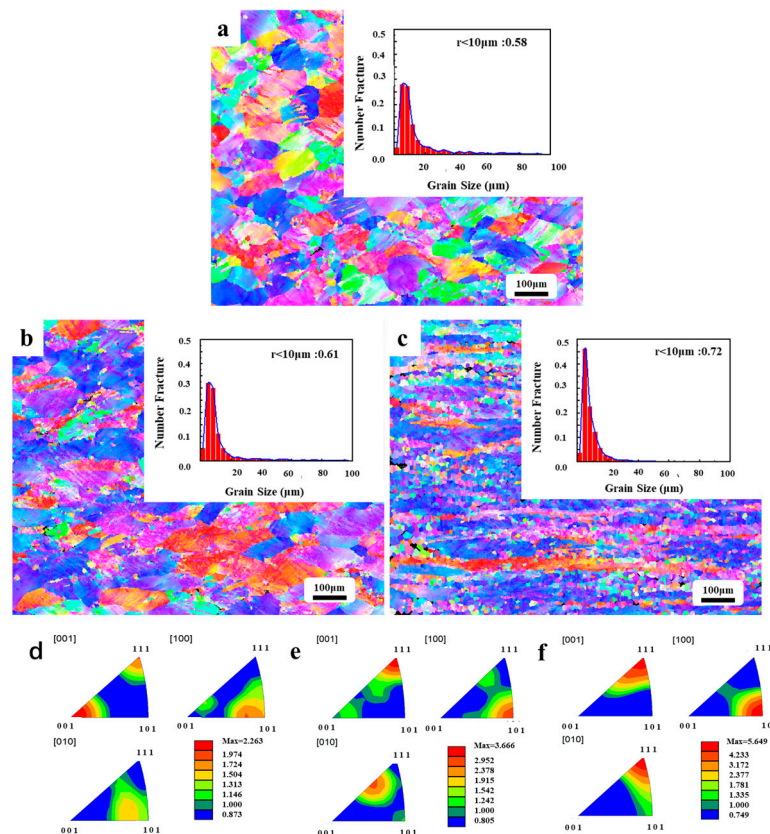


Figure 6. EBSD images of NbHfTiVC_{0.1} of (a,d) 650-30, (b,e) 650-50, (c,f) 650-80; the inserted images show the corresponding grain size distribution plots.

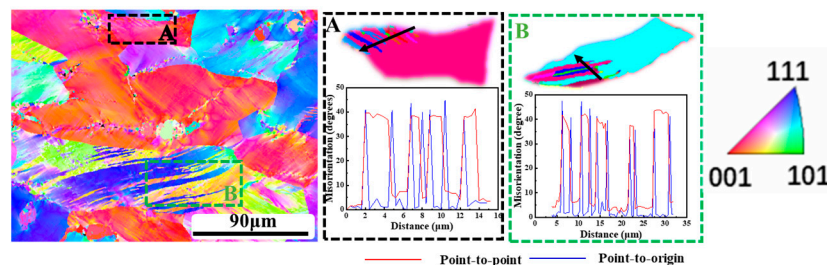


Figure 7. Magnification EBSD map of 650-30; (A,B) are magnification images of areas A and B.

Furthermore, with the increase in rolling reductions, a fraction of small-sized grains (0~10 μm) continuously increased (inserted images in Figure 6a–c), from 0.58 (650-30) to 0.72 (650-80). This indicates that the hot rolling causes an accumulation of stored energy in the grains, which triggers recrystallization. Moreover, the texture intensity increases from 2.36 (650-30 sample) to 5.47 (650-80 sample), and the 650-80 sample leads to the formation of G/B $\langle 101 \rangle$ (111).

Figure 8a–c depicts the distribution of correlated misorientation, and a great number of low-angle grain boundaries (LAGBs) are observed. Specifically, the 650-30, 650-50, and 650-80 samples display proportions of 0.77, 0.780, and 0.833, respectively. The parallel high-angle grain boundaries (HAGBs) (depicted as blue parallel lines) emerge in the hot-rolled samples, facilitating the accumulation of low-angle grain boundaries (LAGBs) between the high-angle twin boundaries. This phenomenon can be attributed to the partial obstruction of dislocation slip by twin boundaries, which consequently leads to the accumulation of dislocations and the formation of sub-grains. The results indicate that with the increase in rolling reductions, both the interface and dislocation strengthening effects improved, consequently resulting in an enhancement of strength.

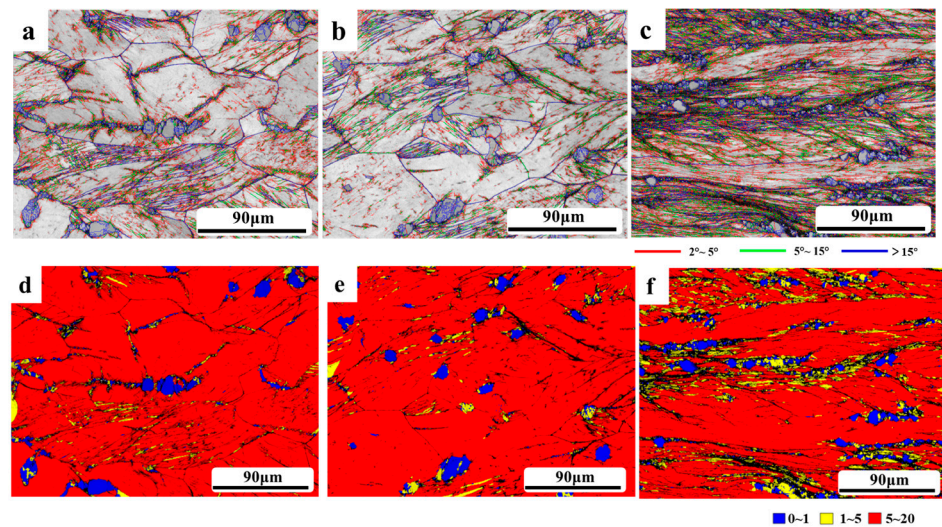


Figure 8. Distribution of correlated misorientations and GOS maps of (a,d) 650-30, (b,e) 650-50, (c,f) 650-80.

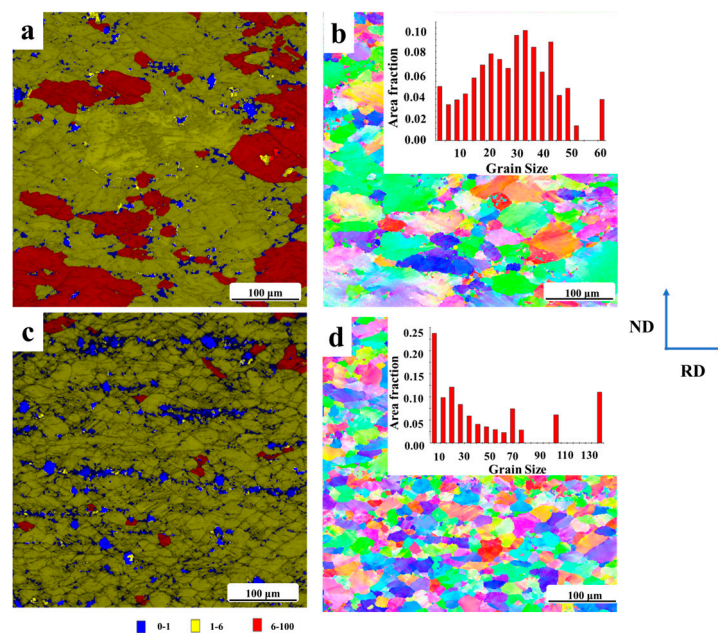


Figure 9. GOS and EBSD maps of (a,b) 1050-50, (c,d) 1050-80; the inserted images show the corresponding grain size distribution plots.

The EBSD-GOS (Grain Orientation Spread Map) is shown in Figure 8d–f. Under lower rolling deformations (30%, 50%), only a portion of the grains undergo recrystallization and are located near the carbides and twinning regions (identified in yellow). However, for 650-80 samples, more recrystallized grains are observed at phase boundaries. Notably, the grains are elongated along the rolling direction and surrounded by partially recrystallized grains, forming a necklace-like structure.

The EBSD-GOS (Grain Orientation Spread Map) is shown in Figure 9a,c. With the increase in rolling reductions, the small-sized grains continued to increase. Under lower rolling deformations (50%), only a portion of the grains undergo recrystallization. However, for the 1050-80 samples, more recrystallized grains are observed, and the proportion of partially recrystallized grains (yellow areas) noticeably increased. The recrystallized grains exhibit elongation parallel to the rolling direction. It indicates that the hot rolling causes an accumulation of stored energy in the grains, which triggers recrystallization. The partially

recrystallized degree is higher than that of the 650 °C hot rolling samples. Notably, more crushed carbides (blue areas) were observed at grain boundaries along the rolling direction.

Furthermore, the EBSD analysis results of the hot-rolled samples at 1050 °C are also studied. The EBSD maps and corresponding grain size distribution plots of the 1050-50 and 1050-80 samples are shown in Figure 9b,d. In the 1050-50 sample, a significant number of equiaxed grains are observed, while a smaller proportion of grains exhibit elongation parallel to the rolling direction. With an increase in rolling reductions, the size of the equiaxed grains continues to decrease. Furthermore, the size distribution of the 1050-80 sample becomes more uniform.

3.2. Mechanical Properties

Figures 10a, 11a, and 12a show a tensile stress–strain curve of the samples, and the ultimate tensile strength and elongation of the samples' fracture are summarized in Table 1. From the results, with an increase in rolling reduction and a rise in temperature, the strength shows significant increases, while there is an increasing trend in plasticity. For the hot rolling at 650 °C and 850 °C, the alloys (650-30, 650-50, 650-70, and 650-80) exhibit a tensile process without yielding or necking stages. The 650-30 sample shows the lowest ultimate tensile strength (UTS) of 705 MPa, while the 650-80 sample exhibits the highest UTS, with a value of 1354 MPa.

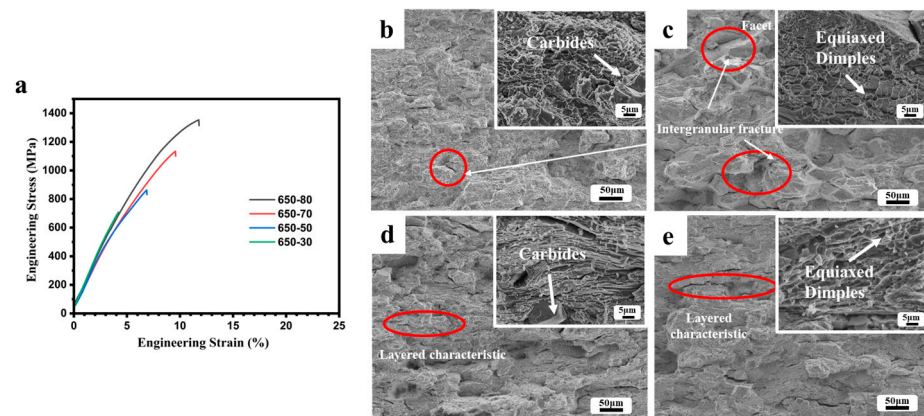


Figure 10. (a) Engineering stress–strain curves of the hot-rolled samples at 650 °C. Fracture surfaces of (b) 650-30, (c) 650-50, (d) 650-70, and (e) 650-80 samples.

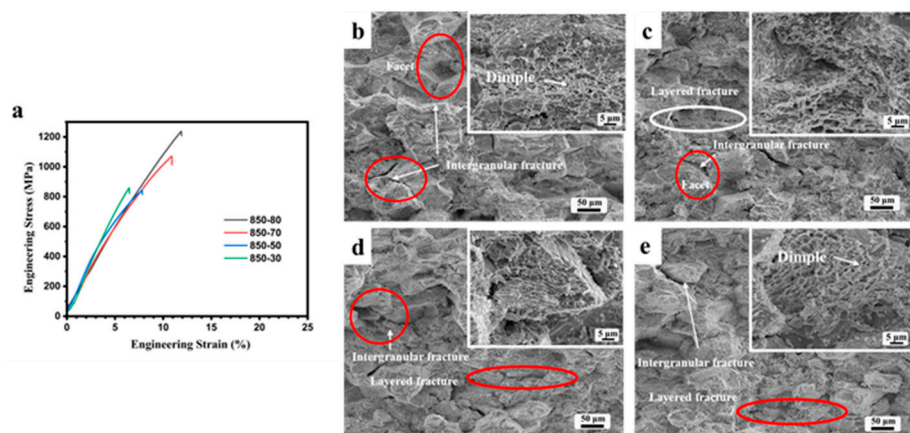


Figure 11. (a) Engineering stress–strain curves of the hot-rolled samples at 850 °C. Fracture surfaces of (b) 850-30, (c) 850-50, (d) 850-70, and (e) 850-80 samples.

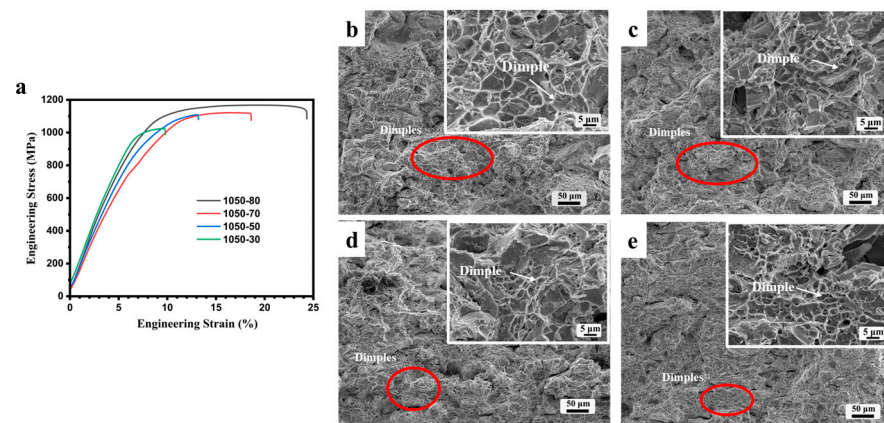


Figure 12. (a) Engineering stress–strain curves of the hot-rolled samples at 1050 °C. Fracture surfaces of (b) 1050-30, (c) 1050-50, (d) 1050-70, and (e) 1050-80 samples.

Table 1. Ultimate tensile strength and elongation of the samples' fracture.

Samples	Ultimate Tensile Strength (MPa)	Elongation to Failure (%)
650-30	705	0
650-50	863	1.5
650-70	1134	1.8
650-80	1354	3.5
850-30	859	1
850-50	843	1.9
850-70	1071	2.3
850-80	1237	1.8
1050-30	1022	3
1050-50	1108	6
1050-70	1118	10
1050-80	1168	16

Unlike the mechanical performance characteristics of the hot-rolled alloys at 650 °C and 850 °C, the alloys demonstrate yield points and uniform deformation stages after being rolled at 1050 °C. Furthermore, the mechanical performance, particularly in terms of ductility, is significantly enhanced. As the rolling reduction increases, the elongation of the alloys also increases, ranging from 3% to 16%. Additionally, with an increase in rolling reductions, the tensile strength of the alloys steadily rises from 1022 MPa to 1168 MPa. A higher degree of partial recrystallisation in the alloys results in a finer microstructure and a more pronounced improvement in plasticity.

The fracture morphology of the hot-rolled alloys at 650 °C is shown in Figure 10b–e. Brittle morphologies of intergranular fracture are exhibited in the 650-30 and 650-50 samples (Figure 10b,c). For the 650-70 sample (Figure 10d), the fracture presented clearly discernible layered characteristics and strip-like dimples, which can be attributed to the significant elongation and deformation of the grains in the direction of rolling. When the amount of rolling deformation reaches 80% (Figure 10e), the fracture also exhibits layered characteristics.

As shown in Figure 11b–e, a typical intergranular fracture with a large number of fine equiaxed dimples and facets is observed in the 850-30 sample, indicating a mixture of brittle and ductile fracture mechanisms. With the increase in rolling reductions (50%, 70%, 80%), layered fractures are observed. The elongated recrystallized grains along the rolling direction result in the layered fracture morphology (Figure 8).

After rolling at 1050 °C, intergranular fracture morphology is no longer observed, and the layered characteristic is not obvious (Figure 12). As reductions increase, the distribution of dimples becomes more uniform, indicating excellent plastic deformation capability.

4. Discussion

4.1. Effect of Hot-Rolled Temperatures on Microstructure of the Samples

BCC, carbide, and Laves phases are observed in the 650 °C and 850 °C hot rolling samples, while only BCC and carbide phases are presented for the 1050 °C hot rolling samples. The numerous nano-sized Laves phase are uniformly dispersed in the BCC matrix with sizes ranging from 200 to 300 nm for 850 °C hot rolling samples, and with sizes less than 100 nm for 650 °C hot rolling samples (Figures 5a and 13a).

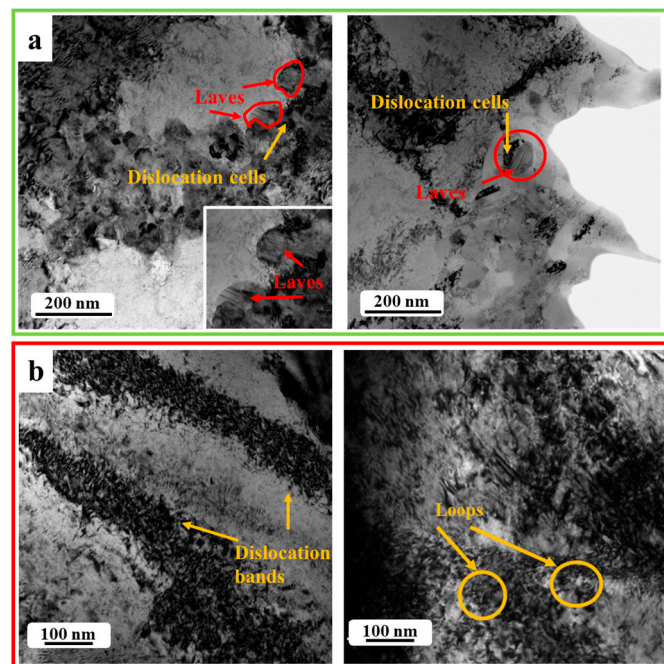


Figure 13. TEM observation: (a) morphology of the interaction between Laves and dislocations for 650-80 sample; (b) the dislocation pattern for 1050-80 sample.

The BCC phase at 650 °C and 850 °C experiences decomposition, resulting in the formation of Laves phases. The diffusion coefficient of solute elements in solids is usually described by the Arrhenius equation [30]:

$$D = D_0 \exp[Q/(RT)] \quad (1)$$

where D_0 denotes the diffusion constant; Q is the activation energy; R is the gas constant; and T is the thermodynamic temperature.

From Equation (1), the solid solubility of secondary phases greatly depends on the temperature. A higher rolling temperature (850 °C) promotes the formation of HfV_2 , resulting in a larger-sized HfV_2 phase formation. Therefore, the size and quantity of the Laves phase for 650 °C hot rolling samples are inferior to those of samples hot rolled at 850 °C. Moreover, due to its smaller size and lower content, the Laves phase cannot be detected via XRD.

From the basic relation, $\Delta G_{\text{mix}} = \Delta H_{\text{mix}} - T\Delta S_{\text{mix}}$ (ΔG_{mix} -free energy, ΔH_{mix} -mixing enthalpy, ΔS_{mix} -mixing entropy, T -temperature), ΔH_{mix} do not change with temperature, which means that the ΔS_{mix} effect becomes the main factor in the equation [40]. The higher temperature (1050 °C) causes an increase in $T\Delta S_{\text{mix}}$, subsequently leading to a decrease in the ΔG_{mix} of the system ($\Delta G_{\text{mix}} = \Delta H_{\text{mix}} - T\Delta S_{\text{mix}}$). The BCC phase becomes more stable, which suppresses the mixing enthalpy (ΔH_{mix}) between V and Hf, thereby inhibiting the precipitation of the Laves phase. Therefore, the Laves phase cannot be observed in the 1050 °C hot rolling sample.

4.2. Strengthening Mechanisms

The highest strength observed in the 650-80 sample results from a combination of dispersion strengthening due to crushed carbide phases and fine Laves phases, as well as fine-grain strengthening within recrystallized grains. During plastic deformation, dislocation tangling and pinning occur, leading to the formation of high-density dislocation cells. The high-density dislocation cells are formed around the Laves phase interface. The interaction between the Laves phase and the high-density dislocation cells can improve deformation resistance. The fine and evenly distributed Laves phases in the BCC matrix hinder the dislocation slip and cause dislocation accumulation and proliferation, thereby greatly improving the strength.

The precipitation strengthening from the Laves and carbide in the 650-80 sample is evaluated using the model from Ref. [41]:

$$\sigma_{ORS} = 0.9M(Gb/L) \frac{R^{3/2}}{R^{3/2} + 2\sqrt{2}} \quad (2)$$

$$R = 2\sqrt{1 - k^2} \quad (3)$$

$$L = 2r \left(\sqrt{\pi/4f} - 1 \right) \quad (4)$$

where L refers to interparticle spacing obtained from the average particle radius r and the particle volume fraction f ; M is the Talyor factor; G is the shear modulus; b is the Burgers vector; and k is a relaxation factor reflecting the particle–matrix interaction.

The strength increment originating from the Orowan mechanism (Equations (2)–(4)) is mainly dependent on r , and is independent of the intrinsic properties of the Laves and carbides. Therefore, there is a negative correlation between the ratio of the strength of alloys and the radii of particles. For the 650-80 sample, the size of the Laves phase (less than 100 nm) is the smallest (Figure 13a). Furthermore, as the deformation increases up to 80%, the crushed carbides become finer ($\sim 5 \mu\text{m}$) and are distributed uniformly along the rolling direction within the matrix. Therefore, the precipitation strengthening produced by the Laves phase and carbides is the strongest.

The grain boundary strengthening mechanism is usually described by the Hall–Petch equation [28]:

$$\sigma_y = \sigma_0 + kD^{-1/2} \quad (5)$$

where σ_y denotes the yield stress, σ_0 is the material constant related to the resistance of lattice to dislocation motion, k is the Hall–Petch strengthening coefficient, and D denotes the average grain size.

The hot rolling process causes a recrystallisation of the sample, leading to decreased grain size ($\sim 10 \mu\text{m}$). The smallest size was observed in the Laves phase and carbides, with the average grain size being the smallest. Therefore, the 650-80 sample exhibits the highest strength.

Large-sized carbides still exist in the 650-30 sample. The occurrence of block-like carbides interspersed among grain boundaries is found to significantly weaken the cohesive strength, ultimately resulting in fracture. Therefore, the 650-30 sample shows the lowest ultimate tensile strength and elongation.

The disappeared Laves phase in the alloy leads to a significant improvement in plasticity for the 1050-80 sample. As indicated in Figure 13b, a large amount of dislocation lines can be seen in the BCC matrix. The BCC phases exhibit parallel dislocation bands, suggesting the occurrence of dislocation slip and the potential to induce stress concentration [42]. The aggregation of dislocations in the dislocation bands inevitably causes dislocation tangles, accompanied by many loops, which slows down the dislocation movement rate. In this case, the occurrence of cross-slip contributes to the stability of plastic deformation. Moreover, frequent slipping is helpful for plastic deformation.

5. Conclusions

In this study, we investigated the microstructure evolution and mechanical properties of NbHfTiVC0.1 refractory high-entropy alloys (RHEAs) during hot rolling. The key findings can be summarized as follows:

- (1) Hot-rolled samples at 650 °C and 850 °C exhibit a composite composition, including BCC, carbide, and Laves phases. However, at 1050 °C, the Laves phase disappears, leaving the samples rolled at this temperature to be composed solely of BCC and carbide phases.
- (2) Increasing the rolling reductions leads to a significant improvement in strength, while increasing rolling temperatures enhances the plastic deformability of the samples. The 650-80 sample displays the highest ultimate tensile strength (1354 MPa), and the 1050-80 sample demonstrates the highest elongation (16%).
- (3) The strength increase observed in the 650 °C hot-rolled sample can be attributed to precipitation strengthening due to crushed carbide phases and fine Laves phases, as well as fine-grain strengthening within recrystallized grains.
- (4) In the case of the 1050 °C hot-rolled sample, the disappearance of the Laves phase results in an increase in ductility. Furthermore, the occurrence of the dislocation slipping mechanism within the BCC matrix also contributes to the enhancement of plastic deformation.

Author Contributions: Conceptualization, B.Z. and S.G.; methodology, W.J.; formal analysis, B.Z., D.W. and X.Y.; investigation, S.W. and X.Y.; data curation, S.W., H.Q. and S.T.; writing—original draft preparation, W.J.; writing—review and editing, S.G. and H.Q.; visualization, S.T.; supervision, B.Z. and D.W.; funding acquisition, W.J. All authors have read and agreed to the published version of the manuscript.

Funding: This research was funded by the Innovation Foundation of GRIMAT Engineering Institute (No.57922102, No.57922201), Youth Fund Project of GRINM (No.66922207) and the State Key Laboratory of Special Rare Metal Materials (No. SKL2021K004), Northwest Rare Metal Materials Research Institute Ningxia Co., Ltd.

Data Availability Statement: Data are contained within the article.

Conflicts of Interest: Authors Haochen Qiu, Shutian Tao, Wei Jiang, Xuehui Yan, Shuai Shuai Wu, Shengli Guo, Baohong Zhu were employed by the companies GRIMAT Engineering Institute Co., Ltd. and China GRINM Group Co., Ltd. Author Dongxin Wang was employed by the company Northwest Rare Metal Materials Research Institute Ningxia Co., Ltd. The remaining authors declare that the research was conducted in the absence of any commercial or financial relationships that could be construed as a potential conflict of interest. The authors declare that this study received funding from the Innovation Foundation of GRIMAT Engineering Institute (No.57922102, No.57922201), Youth Fund Project of GRINM (No.66922207) and the State Key Laboratory of Special Rare Metal Materials (No. SKL2021K004). The funder was not involved in the study design, collection, analysis, interpretation of data, the writing of this article or the decision to submit it for publication.

References

1. Jiang, W.; Shao, W.; Sha, J.B.; Zhou, C.G. Experimental studies and modeling for the transition from internal to external oxidation of three-phase Nb-Si-Cr alloys. *Prog. Nat. Sci. Mater. Int.* **2018**, *28*, 740–748. [[CrossRef](#)]
2. Jiang, W.; Li, M.F.; Sha, J.B.; Zhou, C.G. Microstructure and oxidation resistance of composition gradients Nb-Si based alloy thin film. *Mater. Des.* **2020**, *192*, 108687. [[CrossRef](#)]
3. Li, W.D.; Xi, D.; Li, D.Y.; Zhang, Y.; Gao, Y.F.; Liaw, P.K. Mechanical behavior of high-entropy alloys. *Prog. Mater. Sci.* **2021**, *118*, 100777. [[CrossRef](#)]
4. Yang, W.; Pang, S.J.; Liu, Y.; Wang, Q.; Liaw, P.K.; Zhang, T. Design and properties of novel Ti-Zr-Hf-Nb-Ta high-entropy alloys for biomedical applications. *Intermetallics* **2022**, *141*, 107421. [[CrossRef](#)]
5. Hori, T.; Nagase, T.; Todai, M.; Matsugaki, A.; Nakano, T. Development of non-equiatomic Ti-Nb-Ta-Zr-Mo high-entropy alloys for metallic biomaterials. *Scr. Mater.* **2019**, *172*, 83–87. [[CrossRef](#)]
6. Zhang, H.; Cai, J.L.; Geng, J.L.; Sun, X.Y.; Zhao, Y.Z.; Guo, X.; Li, D.C. Development of high strength high plasticity refractory high entropy alloy based on Mo element optimization and advanced forming process. *Int. J. Refract. Met. Hard Mater.* **2023**, *112*, 106163. [[CrossRef](#)]

7. Chen, Y.W.; Li, Y.K.; Cheng, X.W.; Wu, C.; Cheng, B.; Xu, Z.Q. The Microstructure and Mechanical Properties of Refractory High-Entropy Alloys with High Plasticity. *Materials* **2018**, *11*, 208. [[CrossRef](#)]
8. Sarkar, N.K.; Prajapat, C.L.; Ghosh, P.S.; Garg, N.; Babu, P.D.; Wajhal, P.S.; Krishna, R.; Gonal, M.R.; Tewari, R.; Mishra, P.K. Investigations on superconductivity in an equiatomic disordered Hf-Nb-Ta-Ti-V high entropy alloy. *Intermetallics* **2022**, *144*, 107503. [[CrossRef](#)]
9. Guo, Q.W.; Hou, H.; Pan, Y.; Pei, X.L.; Song, Z.; Liaw, P.K.; Zhao, Y.H. Hardening-softening of Al_{0.3}CoCrFeNi high-entropy alloy under nanoindentation. *Mater. Des.* **2023**, *231*, 112050. [[CrossRef](#)]
10. Chung, T.F.; Chiu, P.H.; Tai, C.L.; Li, Y.L.; Wang, L.M.; Chen, C.Y.; Yeh, J.W.; Hsiao, C.N.; Ou, D.Z.; Wang, S.H.; et al. Investigation on the ballistic induced nanotwinning in the Mn-free Fe₂₇Co₂₄Ni₂₃Cr₂₆ high entropy alloy plate. *Mater. Chem. Phys.* **2021**, *270*, 24707. [[CrossRef](#)]
11. Iijima, Y.; Nagase, T.; Matsugaki, A.; Wang, P.; Ameyama, K.; Nakano, T. Design and development of Ti–Zr–Hf–Nb–Ta–Mo high-entropy alloys for metallic biomaterials. *Mater. Des.* **2021**, *202*, 109548. [[CrossRef](#)]
12. Jiang, W.; Wu, S.S.; Yan, X.H.; Qiu, H.C.; Guo, S.L.; Zhu, B.H.; Zhang, H.J. Impact of Temperature on the Tensile Properties of Hypereutectic High-Entropy Alloys. *COATINGS* **2023**, *13*, 1836. [[CrossRef](#)]
13. He, H.T.; Fang, J.X.; Wang, J.X.; Sun, T.; Yang, Z.; Ma, B.; Chen, H.T.; Wen, M. Carbide-reinforced Re_{0.1}Hf_{0.25}NbTaW_{0.4} refractory high-entropy alloy with excellent room and elevated temperature mechanical properties. *Int. J. Refract. Met. Hard Mater.* **2023**, *116*, 106349. [[CrossRef](#)]
14. Nagase, T.; Todai, M.; Hori, T.; Nakano, T. Microstructure of equiatomic and non-equiatomic Ti-Nb-Ta-Zr-Mo high-entropy alloys for metallic biomaterials. *J. Alloy. Compd.* **2018**, *753*, 412–421. [[CrossRef](#)]
15. Xiang, T.; Du, P.; Cai, Z.; Li, K.; Bao, W.Z.; Yang, X.X.; Xie, G.Q. Phase-tunable equiatomic and non-equiatomic Ti-Zr-Nb-Ta high-entropy alloys with ultrahigh strength for metallic biomaterials. *J. Mater. Sci. Technol.* **2022**, *117*, 196–206. [[CrossRef](#)]
16. Gao, X.J.; Wang, L.; Guo, N.; Luo, L.; Zhu, G.; Shi, C.C.; Su, Y.Q.; Guo, J.J. Microstructure and mechanical properties of multi-phase reinforced Hf-Mo-Nb-Ti-Zr refractory high-entropy alloys. *Int. J. Refract. Met. Hard Mater.* **2022**, *102*, 105723. [[CrossRef](#)]
17. King, D.J.M.; Cheung, S.T.Y.; Humphry-Baker, S.A.; Parkin, C.; Couet, A.; Cortie, M.B.; Lumpkin, G.R.; Middleburgh, S.C.; Knowles, A.J. High temperature, low neutron cross-section high-entropy alloys in the Nb-Ti-V-Zr system. *Acta Mater.* **2019**, *166*, 435–446. [[CrossRef](#)]
18. Stepanov, N.D.; Shaysultanov, D.G.; Salishchev, G.A.; Tikhonovsky, M.A. Structure and mechanical properties of a light-weight AlNbTiV high entropy alloy. *Mater. Lett.* **2015**, *142*, 153–155. [[CrossRef](#)]
19. Čížek, J.; Haušild, P.; Cieslar, M.; Melikhova, O.; Vlasák, T.; Janeček, M.; Kral, R. Strength enhancement of high entropy alloy HfNbTaTiZr by severe plastic deformation. *J. Alloy. Compd.* **2018**, *768*, 924–937. [[CrossRef](#)]
20. Eleti, R.R.; Stepanov, N.; Yurchenko, N.; Klimenko, D.; Zharebtsov, S. Plastic deformation of solid-solution strengthened Hf-Nb-Ta-Ti-Zr body-centered cubic medium/high-entropy alloys. *Scr. Mater.* **2021**, *200*, 113927. [[CrossRef](#)]
21. Senkov, O.N.; Scott, J.M.; Senkova, S.V.; Miracle, D.B.; Woodward, C.F. Microstructure and room temperature properties of a high-entropy TaNbHfZrTi alloy. *J. Alloy. Compd.* **2011**, *509*, 6043–6048. [[CrossRef](#)]
22. Guo, N.N.; Wang, L.; Luo, L.S.; Li, X.Z.; Chen, R.R.; Su, Y.Q.; Guo, J.J.; Fu, H.Z. Microstructure and mechanical properties of in-situ MC-carbide particulates-reinforced refractory high-entropy Mo_{0.5}NbHf_{0.5}ZrTi matrix alloy composite. *Intermetallics* **2016**, *69*, 74–77. [[CrossRef](#)]
23. An, Z.; Mao, S.; Yang, T.; Liu, C.T.; Zhang, B.; Ma, E.; Zhou, H.; Zhang, Z.; Wang, L.H.; Han, X.D. Spinodal-modulated solid solution delivers a strong and ductile refractory high-entropy alloy. *Mater. Horiz.* **2021**, *8*, 948–955. [[CrossRef](#)]
24. Tu, C.H.; Wu, S.K.; Lin, C. A study on severely cold-rolled and intermediate temperature aged HfNbTiZr refractory high-entropy alloy. *Intermetallics* **2020**, *126*, 106935. [[CrossRef](#)]
25. Tang, W.Q.; Zhang, K.; Chen, T.Y.; Wang, Q.; Wei, B.C. Microstructural evolution and energetic characteristics of TiZrHfTa_{0.7}W_{0.3} high-entropy alloy under high strain rates and its application in high-velocity penetration. *J. Mater. Sci. Technol.* **2023**, *132*, 144–153. [[CrossRef](#)]
26. Wei, Q.Q.; Luo, G.Q.; Zhang, J.; Jiang, S.J.; Chen, P.G.; Shen, Q.; Zhang, L.M. Designing high entropy alloy-ceramic eutectic composites of MoNbRe_{0.5}TaW(TiC)_x with high compressive strength. *J. Alloys Compd.* **2020**, *818*, 152846. [[CrossRef](#)]
27. Xu, Z.Q.; Ma, Z.L.; Tan, Y.; Cheng, X.W. Designing TiVNbTaSi refractory high-entropy alloys with ambient tensile ductility. *Scr. Mater.* **2022**, *206*, 114230. [[CrossRef](#)]
28. Zheng, W.J.; Lü, S.L.; Wu, S.S.; Chen, X.H.; Guo, W. Development of MoNbVTax refractory high entropy alloy with high strength at elevated temperature. *Mater. Sci. Eng. A* **2022**, *850*, 143554. [[CrossRef](#)]
29. Tao, S.T.; Jiang, W.; Zhang, W.; Qiu, H.; Wu, S.S.; Guo, S.L.; Zhu, B.H. Microstructure evolution and mechanical properties of NbHfTiVCx novel refractory high entropy alloys with variable carbon content. *J. Alloys Compd.* **2022**, *928*, 166986. [[CrossRef](#)]
30. Jiang, W.; Tao, S.T.; Qiu, H.; Wu, S.S.; Zhu, B.H. Precipitation transformation and strengthening mechanism of droplet ejection lightweight medium-entropy AlZnMgCuLi alloy. *J. Alloy. Compd.* **2022**, *922*, 166152. [[CrossRef](#)]
31. Wei, B.; Tang, B.; Chu, Y.; Du, L.; Chen, X.; Zhu, L.; Li, J.S. The microstructure evolution and tensile properties of Ti–43Al–4Nb–1Mo–0.2B alloy during hot rolling. *Mater. Sci. Eng. A* **2022**, *861*, 144347. [[CrossRef](#)]
32. Han, R.; Yang, G.; Fu, Z.; Xu, D.; Xu, Y.; Zhao, G. Effect of low-temperature hot rolling on the microstructure and mechanical properties of air-cooling medium manganese martensitic wear-resistant steel. *Mater. Charact.* **2023**, *203*, 113139. [[CrossRef](#)]

33. Zhu, Z.Y.; Liu, Y.L.; Gou, G.Q.; Gao, W.; Chen, J. Effect of heat input on interfacial characterization of the butter joint of hot-rolling CP-Ti/Q235 bimetallic sheets by Laser + CMT. *Nat. Publ. Group* **2021**, *11*, 10020. [[CrossRef](#)] [[PubMed](#)]
34. Yan, Y.W.; Li, G.R.; Ren, W.X.; Wang, H.; Gao, L.P. Effects of hot rolling on microstructure and properties of FeCoNi_{1.5}CrCu/2024Al composites. *J. Alloy. Compd.* **2022**, *900*, 163393. [[CrossRef](#)]
35. Wu, M.; Yang, C.; Kuijter, M.; Baker, I. Enhanced mechanical properties of carbon-doped FeNiMnAlCr high entropy alloy via hot-rolling. *Mater. Charact.* **2019**, *158*, 109983. [[CrossRef](#)]
36. Liu, Z.; Xiong, Z.P.; Chen, K.X.; Cheng, X.W. Large-size high-strength and high-ductility AlCoCrFeNi_{2.1} eutectic high-entropy alloy produced by hot-rolling and subsequent aging. *Mater. Lett.* **2022**, *315*, 131933. [[CrossRef](#)]
37. Zhuang, W.C.; Huang, Z.Y.; Hu, W.Q.; Yu, Q.; Wang, H.; Li, X.; Wu, Y.B.; Zhou, Y. Study of microstructure and mechanical properties of quasi-continuous network structured (Ti₃AlC₂-Al₃Ti)/2024Al composites based on hot rolling. *J. Alloys Compd.* **2023**, *968*, 171936. [[CrossRef](#)]
38. Cui, C.Y.; Cao, G.M.; Li, X.; Gao, Z.; Zhou, X.; Liu, Z.Y. The coupling machine learning for microstructural evolution and rolling force during hot strip rolling of steels. *J. Mater. Process. Technol.* **2022**, *309*, 117736. [[CrossRef](#)]
39. GB/T 228.1-2010; Metallic Materials-Tensile Testing-Part 1: Methods of Test at Room Temperature. China National Standardization Management Committee: Beijing, China, 2010.
40. Chen, S.Y.; Tong, Y.; Tseng, K.K.; Yeh, J.W.; Poplawsky, J.D.; Wen, J.G.; Gao, M.C.; Kim, G.; Chen, W.; Ren, Y.; et al. Phase transformations of HfNbTaTiZr high-entropy alloy at intermediate temperatures. *Scr. Mater.* **2019**, *158*, 50–56. [[CrossRef](#)]
41. Moravcik, I.; Hornik, V.; Minarik, P.; Li, L.L.; Dlouhy, I.; Janovska, M.; Raabe, D.; Li, Z.M. Interstitial doping enhances the strength-ductility synergy in a CoCrN in medium entropy alloy. *Mater. Sci. Eng. A* **2020**, *781*, 139242. [[CrossRef](#)]
42. Yan, X.H.; Liaw, K.P.; Zhang, Y. Ultrastrong and ductile BCC high-entropy alloys with low-density via dislocation regulation and nanoprecipitates. *J. Mater. Sci. Technol.* **2022**, *110*, 109–116. [[CrossRef](#)]

Disclaimer/Publisher's Note: The statements, opinions and data contained in all publications are solely those of the individual author(s) and contributor(s) and not of MDPI and/or the editor(s). MDPI and/or the editor(s) disclaim responsibility for any injury to people or property resulting from any ideas, methods, instructions or products referred to in the content.